Chapter 4

Results and Discussion

4.1 Raw material characterization

4.1.1 Phase analysis

The phases of as-received raw materials were determined by XRD. The XRD results of $SrCO_3$ and Al_2O_3 as illustrated in Fig 4.1 showed their own single phase, corresponding to the JCPDS no. 05-0418 and no. 43-1484, respectively. The XRD patterns of La_2O_3 and MgO showed the impurity phase. The extra peaks found in as-received La_2O_3 could be observed at 2θ 27°, 28° and 47°, corresponding to JCPDS no. 36-1481 of $La(OH)_3$. The XRD result of MgO revealed the small peaks of $Mg(OH)_2$ at 2θ 18°, 38° and 51°(JCPDS no. 07-0239). These indicated that La_2O_3 and MgO easily absorbed moisture from the air to form hydroxide. To obtain accurate content of La_2O_3 and MgO, the as-received La_2O_3 and MgO were calcined before introduced as starting materials for sample preparation.

4.1.2 Thermal analysis of as-received La_2O_3 and MgO

Hydroxide found in commercial La_2O_3 and MgO could cause the deviation from the desired composition. To eliminate the hydroxide, the calcination of as-received La_2O_3 and MgO was necessary. The DTA and TGA were used to determine the appropriate firing schedule. The resulting curves of La_2O_3 and MgO were illustrated in Fig 4.2.

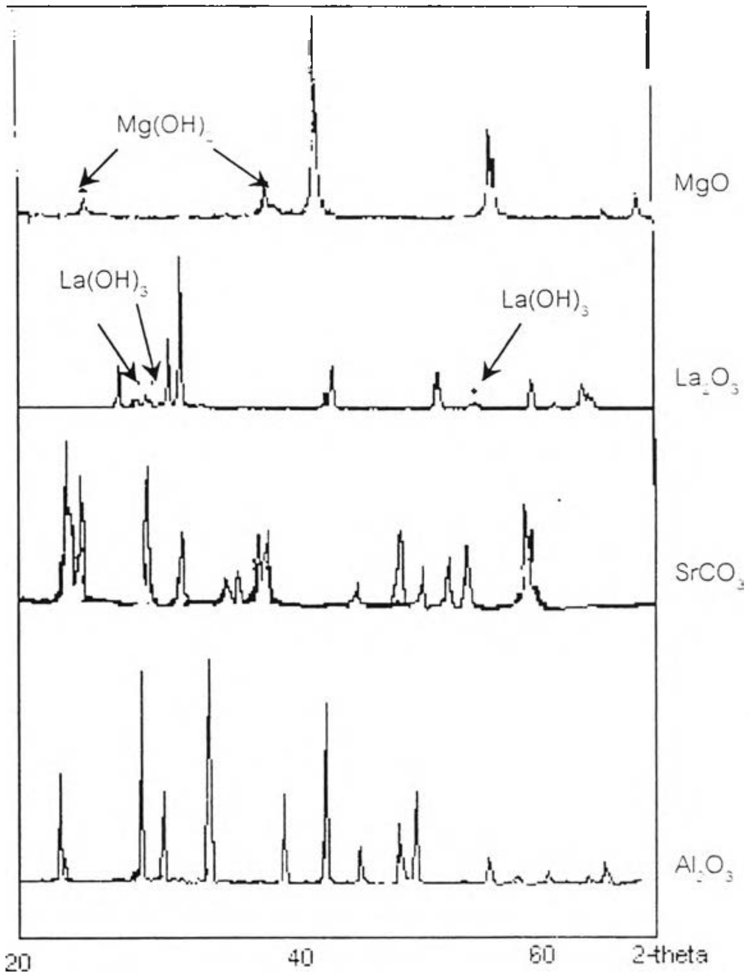

Fig 4.1 XRD patterns of received raw materials

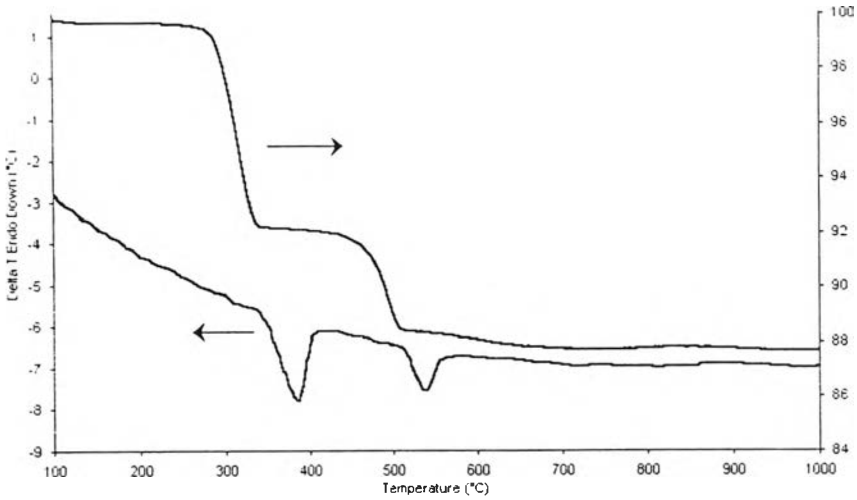

(a)

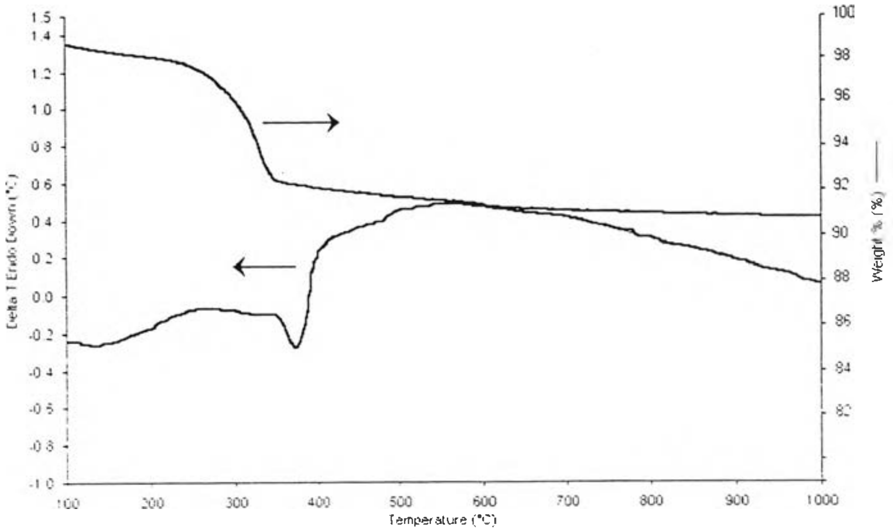

(b)

Fig 4.2 DTA and TGA traces of as-received (a) La_2O_3 and (b) MgO

According to Fig 4.2 (a), there were two endothermic peaks at 344°C and 514°C, corresponding to TGA result. Similarly, TGA curve of MgO raw material in Fig 4.2 (b) showed the weight loss around 350°C, corresponding to the endothermic process of the DTA curve. These peaks probably represented the decomposition of hydroxide.

From these results, the firing schedule of La_2O_3 and MgO raw materials as shown in Fig 4.3 was set up. The maximum temperature was 1000°C along with the soaking time at each reaction temperature. After calcining, there was no $La(OH)_3$ and $Mg(OH)_2$ left as appeared from XRD results in Fig. 4.4.

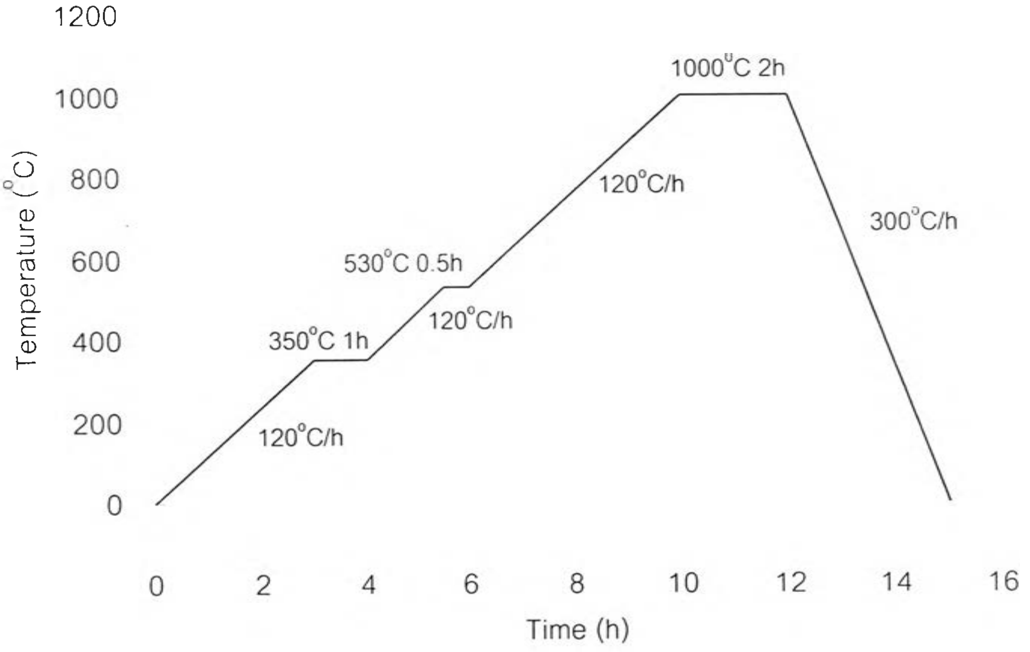

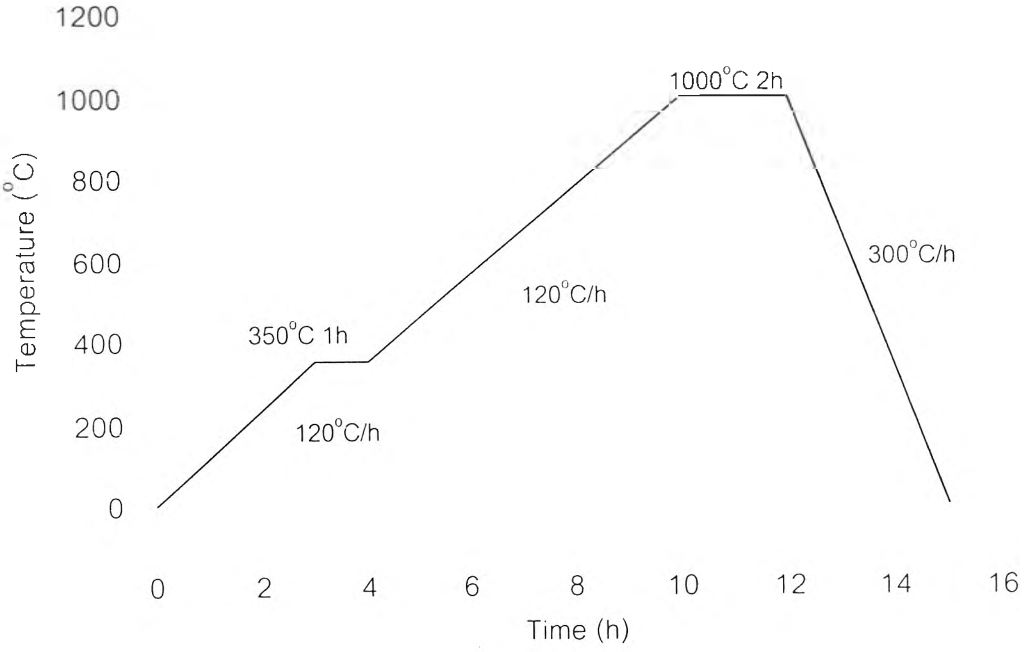

Fig 4.3 Firing schedule of as-received (a) La_2O_3 and (b) MgO

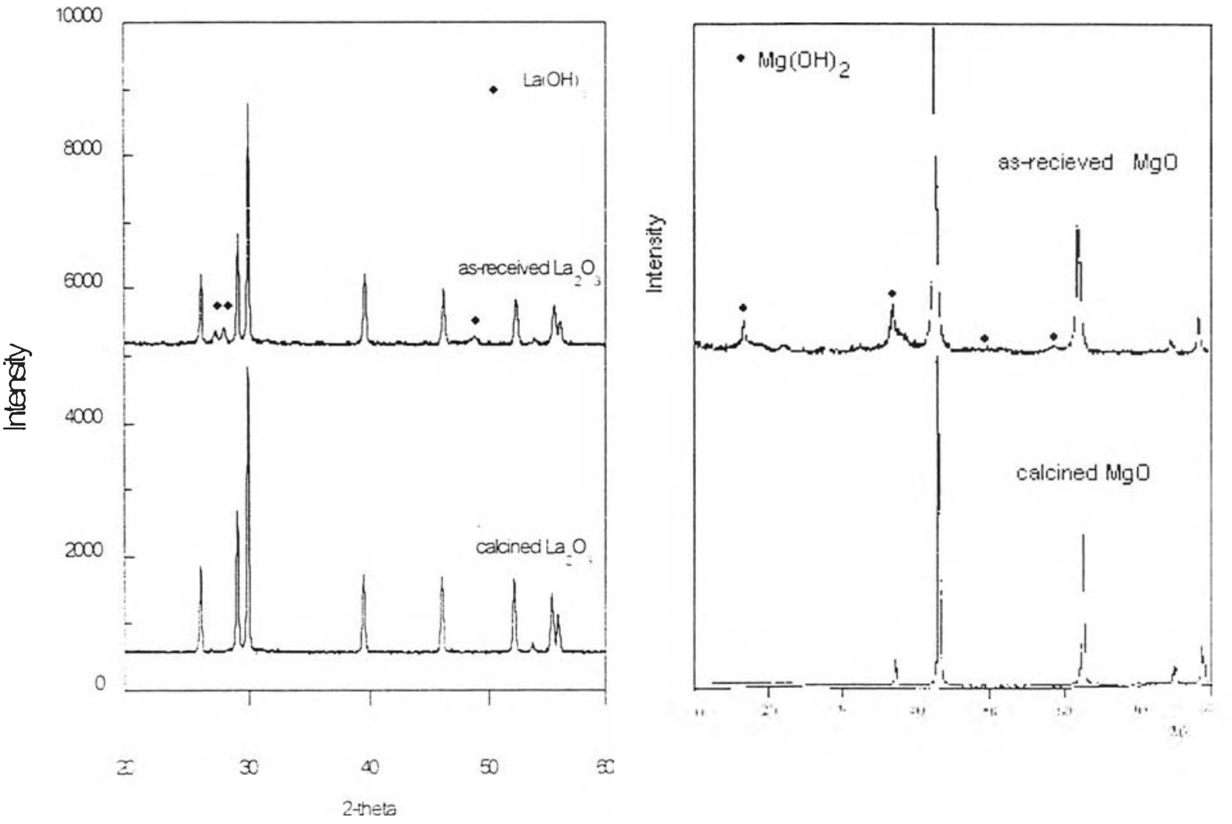

(a)

(b)

Fig 4.4 XRD patterns of as-received and calcined (a) La$_2$O$_3$ and (b) MgO

4.2 Determination of calcining temperature for $La_{1-x}Sr_xAl_{1-y}Mg_yO_{3-\delta}$

Fig 4.5 showed the DTA results of std, S15, and M15 from 100°C to 1200°C. They all appeared the same characteristics. Expectedly, the reaction peaks of the compositions the range between std and S15 or M15 should be the same. Therefore, these results also used as the representative of the compositions S5, S10, M5, and M10.

There were two steps of endothermic processes at 350-380°C and 530-550°C. Also the exothermic peak occurred at 470-480°C; it probably related to the structural transition from rhombohedral to cubic perovskite. This result was in good agreement to that reported by the earlier studies (8,19-22). Gellar and Bala observed that the lanthanum aluminate perovskite structure was rhombohedral at room temperature and transformed to cubic above 435°C. However, an accurate determination of the transition temperature could not be conducted. H.M. O'bryan et al.(21) reported that transition temperature was near 500°C. From this result, the firing schedule of all compositions was set up and illustrated in Fig 4.6. Although the reaction peak could be observed at 700-1200°C, XRD pattern of powder calcined at 1200°C showed the second phase. Thus the powder mixture of all compositions was calcined at 1350°C. The calcination was necessary to be repeated at the same condition to obtain homogeneous composition. Thus the XRD patterns of std, S5, S10, and S15 as shown in Fig 4.7 confirmed that the perovskite single phase was obtained. However, the XRD results of Mg modified S10 showed some second phase and the amount of the second phase increased with the increasing of Mg content.

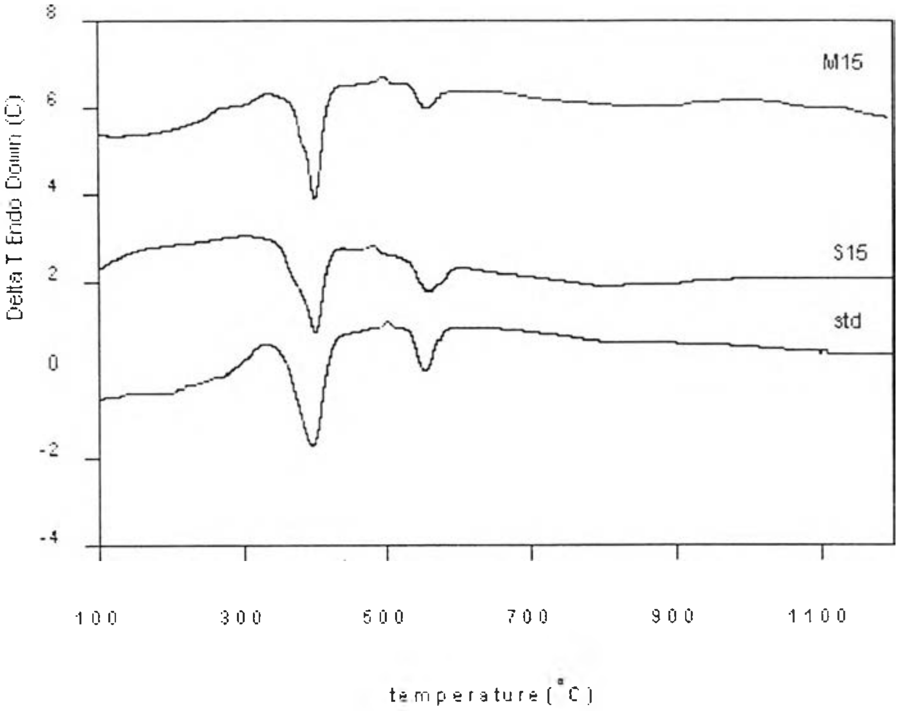

Fig 4.5 DTA curves of $LaAlO_3$ (std), $La_{0.85}Sr_{0.15}AlO_{2.925}$ (S15) and $La_{0.9}Sr_{0.1}Al_{0.85}Mg_{0.15}O_{2.875}$ (M15)

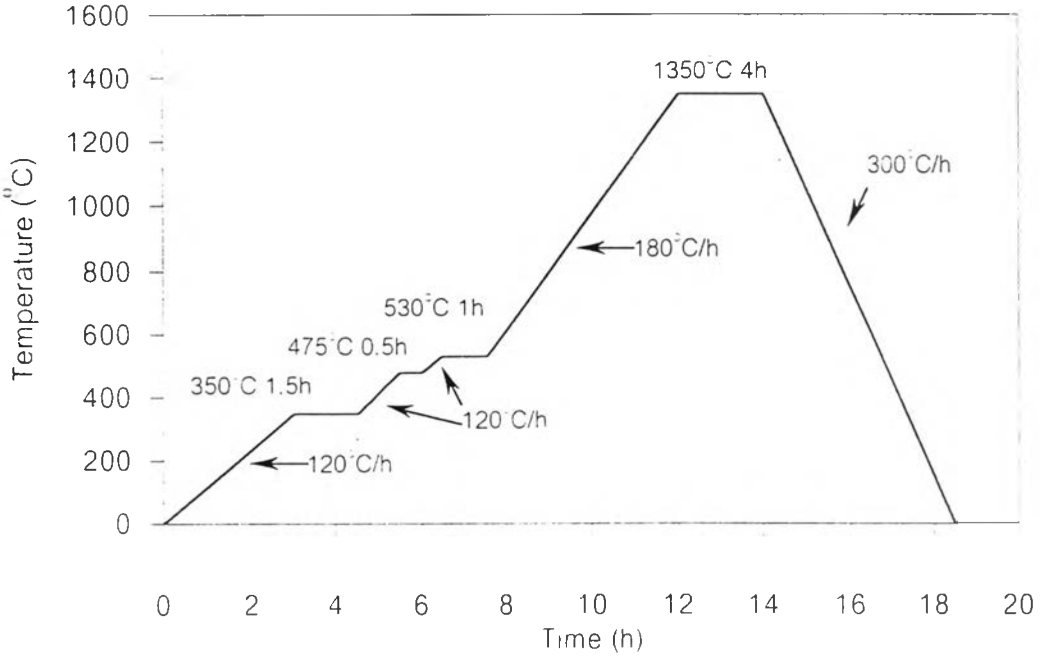

Fig 4.6 Firing schedule of all compositions

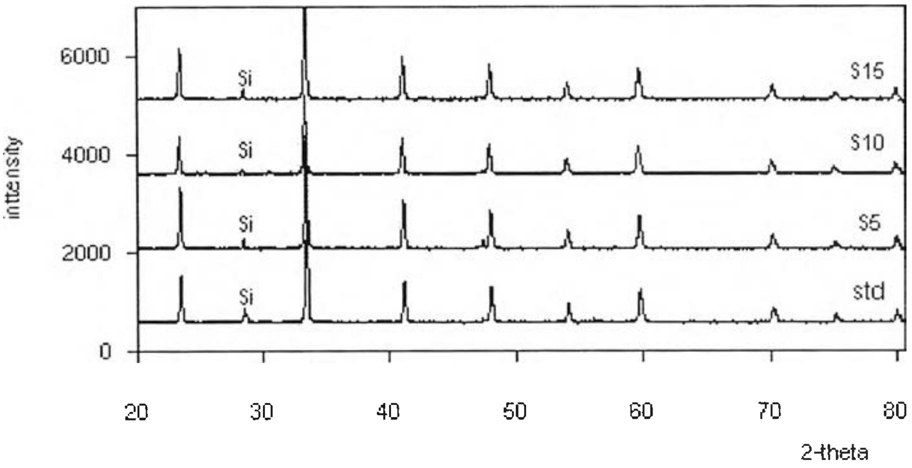

Fig 4.7 XRD patterns of std, S5, S10 and S15 calcined at 1350°C for 4 hours

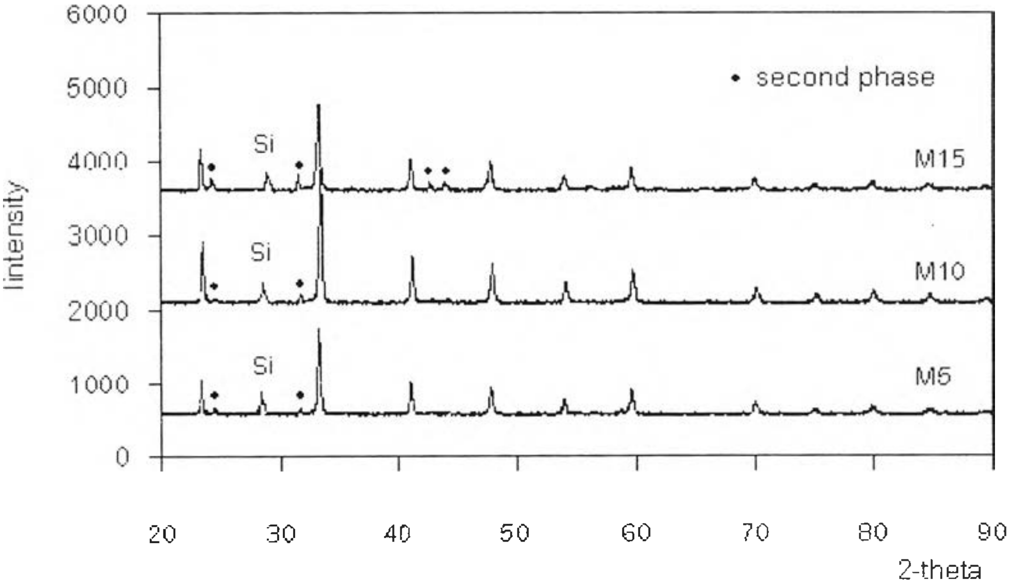

Fig.4.8 XRD patterns of Mg doped in S10 calcined at 1350°C for 4 hours

4.3 Determination of $LaAlO_3$ structure

The calcined powder was mixed with Si used for an internal standard to calibrate the d-spacing values. Many controversies in the structure of lanthanum aluminate were reported. Many researchers have observed that lanthanum aluminate (with or without dopant) posses rhombohedral structure, corresponding to JCPDS no. 32-0022, however, the cubic structure was also reported by P.S. Anderson et al (9). In this study, although it was looked like the cubic so-called pseudocubic, most perovskite compounds always had the distortion in their structure obtained from either the dopants or the synthesized processing. To detect the structure distortion of $LaAlO_3$ and its modifications, the line splitting of (220) reflection was observed around 70° 2θ. Theoretically, the splitting of (220) could be seen clearly in rhombohedral but not cubic. The XRD data of std calcined powder were collected in the range of 2θ 69.5-71°using the slow step scan of 0.01° and the long count time of 6 sec. As seen from the result in Fig 4.9 the splitting of (220) could not be observed clearly and this implied that its structure was either cubic or rhombohedral in which α was closed to 90°. If $LaAlO_3$ responded to an electric field, the (220) reflection would be splitted after an electric field was applied. However, this was beyond the objective of this research.

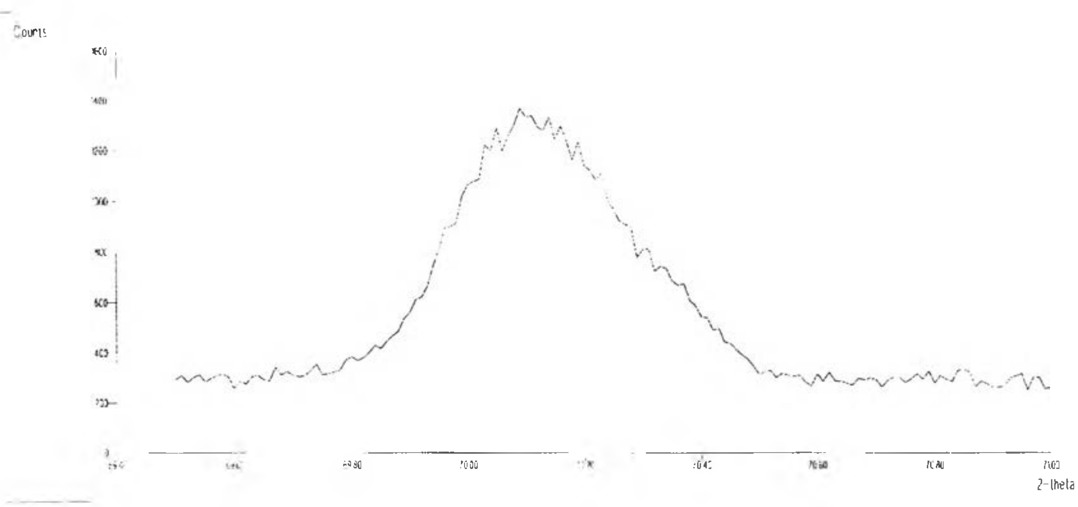

Fig 4.9 XRD pattern of std calcined at 1350°C for 4 hours

Table 4.1 showed the 2θ and d spacing from the XRD measurement of the undoped $LaAlO_3$ composition as compared to 2θ which was calculated from cubic structure. The $2\theta_{cal}$ was derived from equations 4.1 and 4.2.

$$\lambda = 2d\sin\theta \tag{4.1}$$

$$\frac{1}{d^2} = \frac{(h^2 + k^2 + l^2)}{a^2} \tag{4.2}$$

Where λ is the wavelength of Cu (1.54056 Å) and a is the lattice parameter of $LaAlO_3$ (3.79 Å) could be calculated from (100).

The $2\theta_{cal}$ slightly deviated from $2\theta_{obs}$, suggesting that the structure should not be cubic.

Table 4.1 The XRD data of std

h k l	$2\theta_{obs}$	$2\theta_{ca}$	d_{obs}	I/I_0
1 0 0	23.443	23.443	3.783	48
1 1 0	33.383	33.395	2.677	100
1 1 1	41.183	41.206	2.187	43
2 0 0	47.943	47.941	1.894	37
2 1 0	54.023	54.039	1.694	21
2 1 1	59.663	59.689	1.547	33
2 2 0	70.143	70.149	1.340	17
2 2 1	75.063	75.10	1.263	10

However the lattice parameter reported in this thesis was determined by a cubic approximation since the angular distortion was less and insignificantly influence.

4.4 Effects of dopant on structural parameter of calcined powder

The results of XRD patterns for std, S5, S10, and S15 shown in Fig 4.7 suggested that they all exhibited the same structure. The lattice parameter and X-ray density of these compositions were calculated after correction with Si standard and determined by cubic approximation. These results were summarized in Table 4.2.

The XRD patterns of Mg doped in S10 were shown in Fig 4.8. The unknown peaks exhibited and the number of peaks increased with an increasing amount of Mg. Although there were second phases in Mg modified S10, the lattice parameter was attempted to calculate from the main peaks and the extra peaks were not concerned in this study.

Table 4.2 The lattice parameter determined by cubic approximation and X-ray density of all compositions

Composition	Symmetry	Lattice Parameter (Å)	Cell volume (Å)^3	X-ray density (g/cm^3)
Std.	Pseudo-Cubic	3.787	54.31	6.54
S5	Pseudo-Cubic	3.786	54.27	6.44
S10	Pseudo-Cubic	3.788	54.35	6.32
S15	Pseudo-Cubic	3.792	54.53	6.24
M5	Pseudo-Cubic	3.797	54.74	6.30
M10	Pseudo-Cubic	3.799	54.83	6.33
M15	Pseudo-Cubic	3.801	54.92	6.22

Table 4.3 Ionic radii (22)

Ion	Radius (Å)
La^{3-}	1.36
Al^{3-}	0.53
Mg^{2-}	0.72
Sr^{2-}	1.46

The substitution of cation with 2+ into that of 3+ created the oxygen vacancies resulting in a decreasing of lattice parameter. However, the results showed in Tables 4.2 revealed that the cell volume increased with an increasing amount of 2+ cation. The only one oxygen vacancy occurred when replacing two trivalent cations with two divalent cations. This result may imply that the effect of cation size on the cell volume was stronger than the existence of oxygen vacancies. From Table 4.2, the lattice parameter of Sr^{2-} doped $LaAlO_3$ increased with slightly increasing of dopant concentration because ion radius of Sr^{2-} was larger than that of La^{3-}. The larger ionic radius of Mg^{2-} than Al^{3-} attributed to the lattice parameter of M5, M10, and M15 were larger than S10 as represented in Table 4.3. The unit cell increased with the amount of Mg dopant. In addition, the lattice parameter increased significantly with Mg substitution as compared to Sr substitution.

4.5 Effect of dopant on properties of specimens after sintering

4.5.1 Phase analysis

The specimens prepared from perovskite oxide powder were sintered at 1500°C for std and S5. The bulk density of S10 and S15 was too low if they were sintered at 1500°C and 1550°C (see section 4.5.2). To obtain dense pellets, S10 and S15 were sintered at 1575°C. The phase of the sintered specimens was determined by XRD and shown in Fig 4.10. It was evident that there were slightly unknown peaks shown at 2θ 45° in all compositions. However the amount of second phase was less and may be caused by inappropriate sintering temperature and soaking time.

The XRD patterns of Mg-modified S10 were illustrated in Fig 4.11. As seen from XRD results of M5, the extra peak existed at 2θ 45° which could be observed in S10. The XRD patterns of M10 and M15 showed that the peak at 2θ 45° disappeared and the extra peak occurred at 2θ 31°. This was possibly because the substitution of Mg decreased the sintering temperature. Although, with the amount of Mg up to 10-15mol%, the second phase observed in both S10 and M5 dissolved, the segregation of other phase took place due to over limitation of the solid solution of M10 and M15.

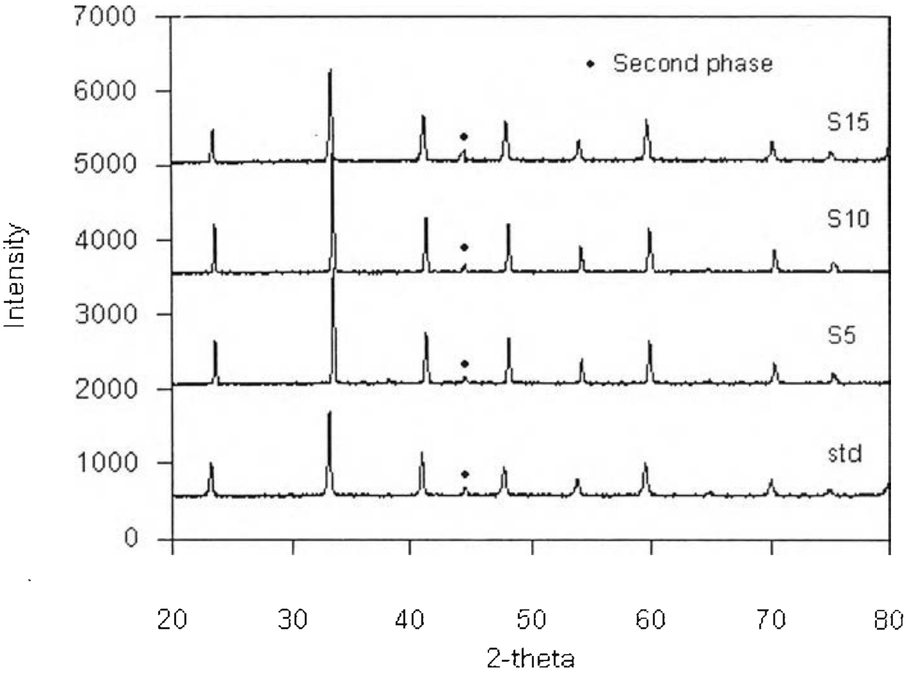

Fig 4.10 XRD patterns of std and S5 sintered at 1500°C and S10 and S15 sintered at 1575°C

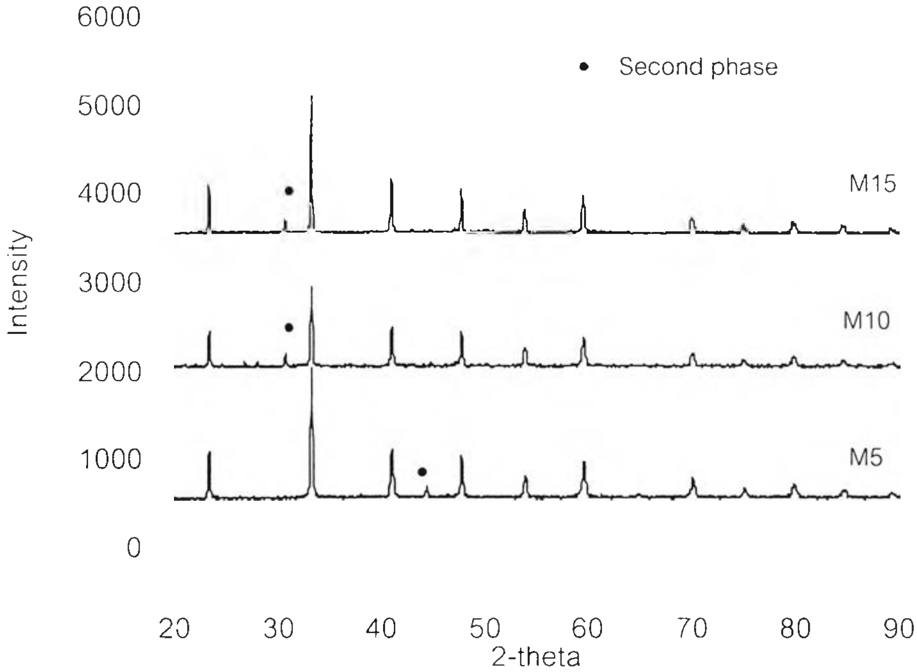

Fig 4.11 XRD patterns of M5, M10 and M15 sintered at 1575°C

4.5.2 Density

The bulk density of the pellets sintered at various temperatures was determined by Archimedes method and summarized in Table 4.4. It was clearly seen that the density decreased with the increasing amount of Sr but increased with the increasing amount of Mg at the same sintering temperature. Therefore, the high sintering temperature was required for Sr-doped composition. The structural parameter of M15 was not correct because the amount of the impurity phases was very high. To obtain higher density, the sintering temperature of S10, S15, M5, M10 and M15 were set up to 1575°C. Higher temperature than 1575°C was not able to approach because of the limitation of existing furnace in the laboratory. This should be noted that the percentage of the theoretical density was not calculated due to the existence of other phases in the composition.

Table 4.4 Density of sintered samples

Composition	Sintering Temperature	X-ray density (g/cm^3)	Bulk Density (g/cm^3)
Std	1500	6.54	6.33±0.07
S5	1500	6.44	6.21±0.08
S10	1500	6.32	4.96±0.03
S10	1550	6.32	5.04±0.05
S10	1575	6.32	5.21±0.06
S15	1500	6.24	4.77±0.02
S15	1550	6.24	5.01±0.02
S15	1575	6.24	5.92±0.05
M5	1575	6.30	5.75±0.08
M10	1575	6.33	5.85±0.09
M15	1575	6.22	5.90±0.07

4.5.3 Electrical conductivity

In general, the electrical conductivity (σ) of the material depends on the temperature and can be expressed by Arrhenius equation as follows

$$\sigma = \frac{A}{T}\exp\left[\frac{-E_a}{kT}\right] \quad (4.3)$$

where T is the absolute temperature and k is the Boltzmann constant. E_a is activation energy (kJ/mol) and A is the pre-exponential constant. E_a is derived from the slope of Arrhenius plot between 1/T vs. log (σT) on the x and y-axis, respectively.

a) DC four point method

The electrical conductivity of rectangular bars sintered at 1500°C for std. and S5, and 1575°C for S10 and S15 was measured as a function of temperature. The gold electrode was applied on the sample for electrical contact before measurement. Since undoped $LaAlO_3$ was very resistive material, the conductivity could be measured at the temperature above 800°C. From this result, the Arrhenius plot could not be obtained and the dc conductivity of undoped was not shown. The plots of log (σT) and 1/T of S5 sintered at 1500°C, S10 and S15 sintered at 1575°C were illustrated in Fig 4.12. As seen from this figure, the plot form each composition exhibited two slopes to obtain a regression coefficient greater than 0.997, the two regions of each composition were seperated as appeared in Fig 4.13. This straight line equation of each region was determined from the fitting program and also given in Fig 4.13. The calculated activation energy was summarized in Table 4.5.

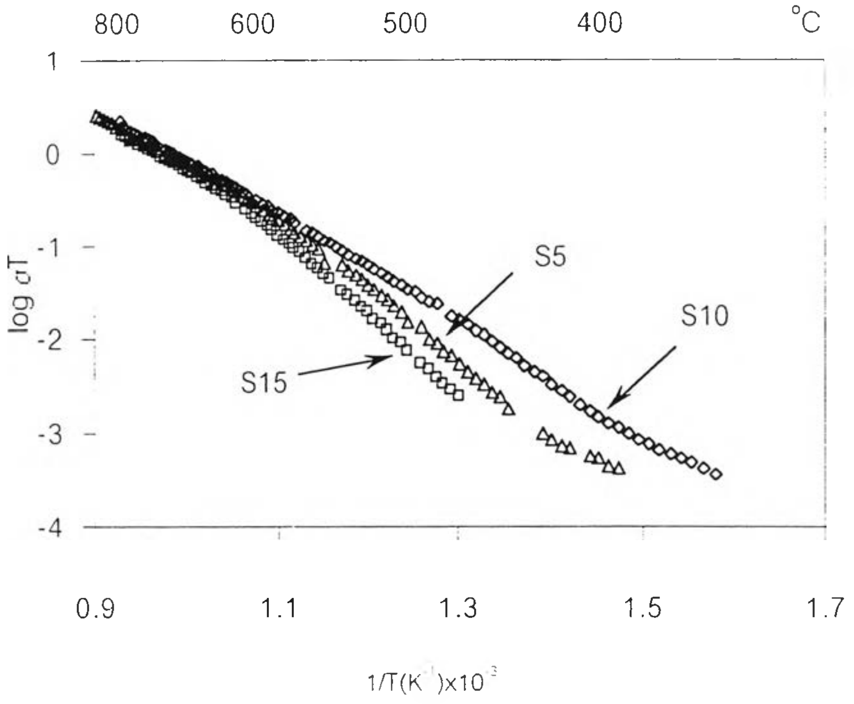

Fig. 4.12 Electrical conductivity vs reciprocal temperature of S5 sintered at 1500°C, S10 and S15 sintered at 1575°C

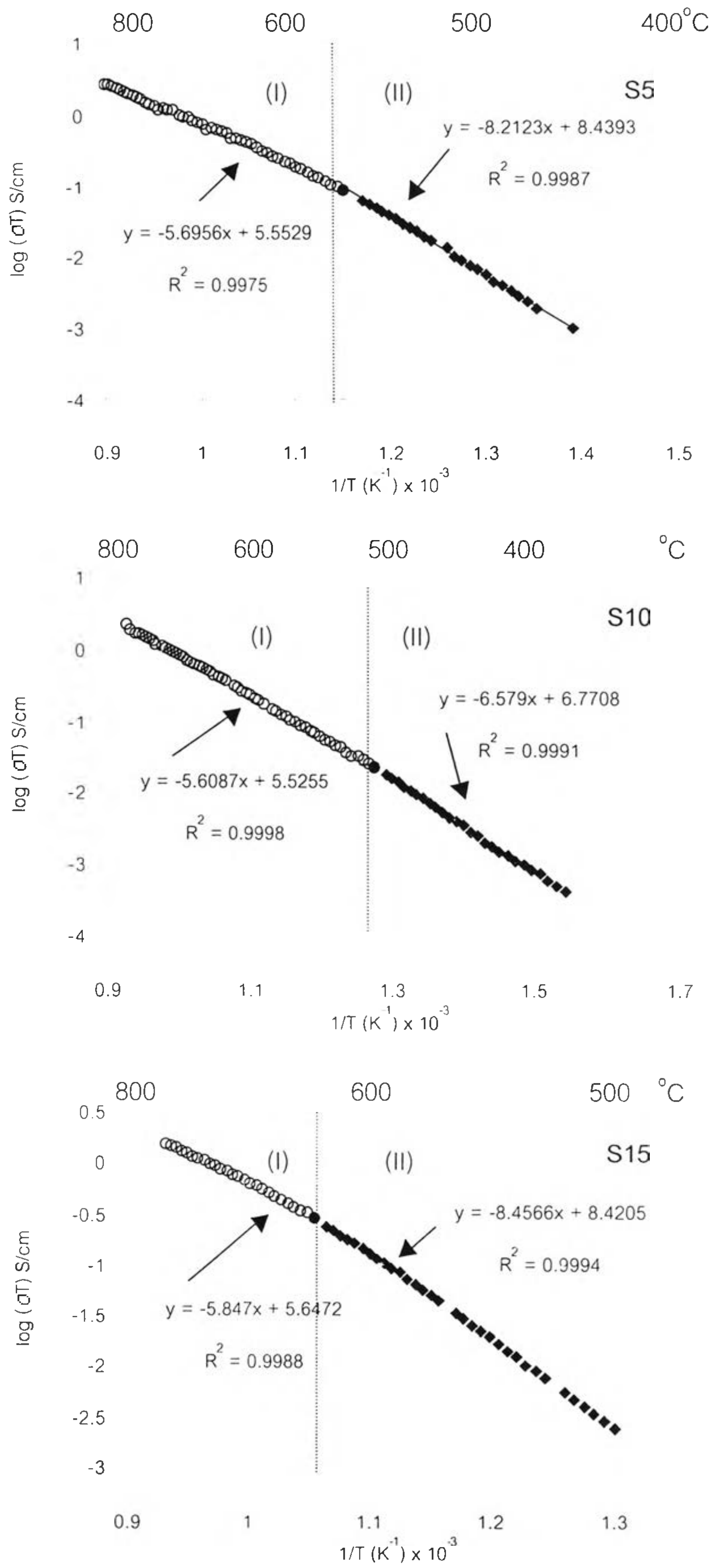

Fig 4.13 Electrical conductivity vs. reciprocal temperature of S5, S10 and S15 illustrated the two regions

Table 4.5 Calculated activation energy of S5, S10 and S15

Composition	Temperature range (°C)	E_a (kJ/mol)
S5	350-580	158
	580-800	109
S10	350-510	126
	510-800	107
S15	350-620	162
	620-800	112

The calculated activation energy deceased with the increasing of temperature. This result agreed with the works of the previous studies (8,9,12,23). This characteristic commonly observed in other ionic conductor. The apparent activation energy (E_a) is expressed by the sum of a migration enthalpy (ΔH_m) and the dopant-vancacy association enthalpy (ΔH_a). At low temperature, both are present but with increasing temperature the coulombic forces between positive (oxygen vacancies) and negative defect (A and B site dopant) decrease due to increased thermal energy leaving only ΔH_m at the elevated temperature. From this result, the activation energy at the high temperature was lower than that in the low temperature. In addition, Nomura K.(8) suggested that the symmetry of the $(La_{1-x}Sr_x)MO_{3-\delta}$ compound where M was Al, Ga, Sc, In and Lu was presumed to increase gradually due to the phase transition from rhombohedral to cubic. As a result, the activation energy of ion for migration decreased. In addition, S10 had the lowest activation energy of 126 and 107 kJ/mol. The σ_{1000} and σ_{800} were calculated from the Arrhenious plot in the region (I) and showed in Table 4.6. S10 had the highest electrical conductivity at 1000°C of 10.35×10^{-3} S/cm and at 800°C of 1.85×10^{-3} S/cm.

Table 4.6 Calculated σ_{1000} and σ_{800} of S5, S10 and S15

Composition	σ_{1000}(S/cm)	σ_{800}(S/cm)
S5	9.42×10^{-3}	1.64×10^{-3}
S10	10.35×10^{-3}	1.85×10^{-3}
S15	8.90×10^{-3}	1.47×10^{-3}

b) AC impedance spectroscopy

The results of AC impedance as a function of temperature of std were shown in Fig 4.14(a) and (b). The curves of all measuring temperature except at 900°C did not intercept the z' axis resulting from very high resistance of this composition. At 900°C, the curve intercept the z' axis at 450 kohm. However, the plot tended to form a single semi-circle at high temperature as observed in Fig 4.14(b).

Fig 4.15 illustrated the effect of temperature on the resistance of S10. The resistance decreased with the increasing of temperature. This characteristic could be observed in all compositions.

The density of the pellet affected the resistance of the sample. As Shown in Fig 4.16, when the density increased, the resistance decreased.

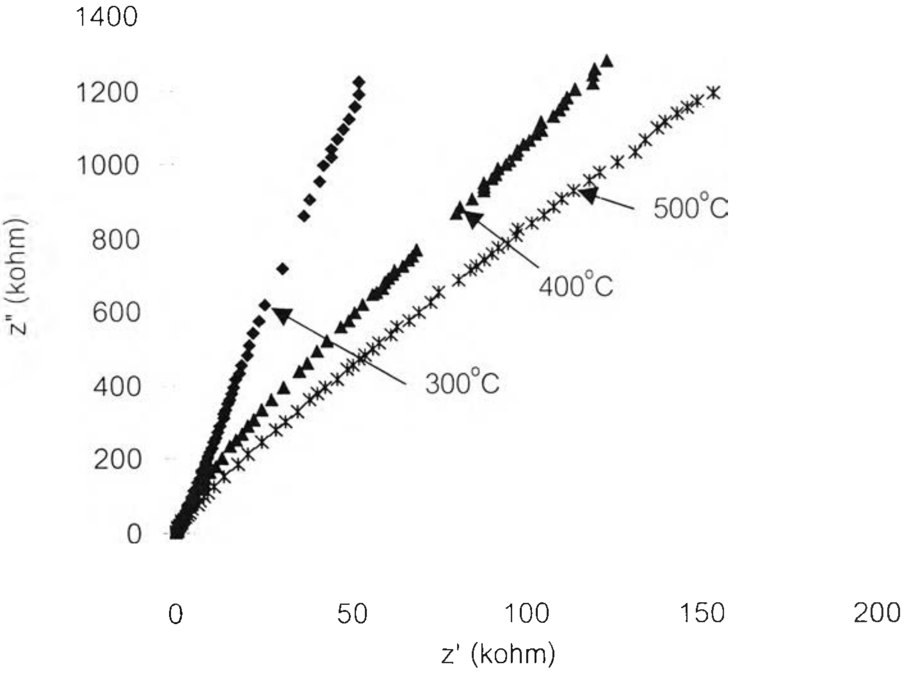

Fig.4.14(a) Impedance plots of std at 300-500°C

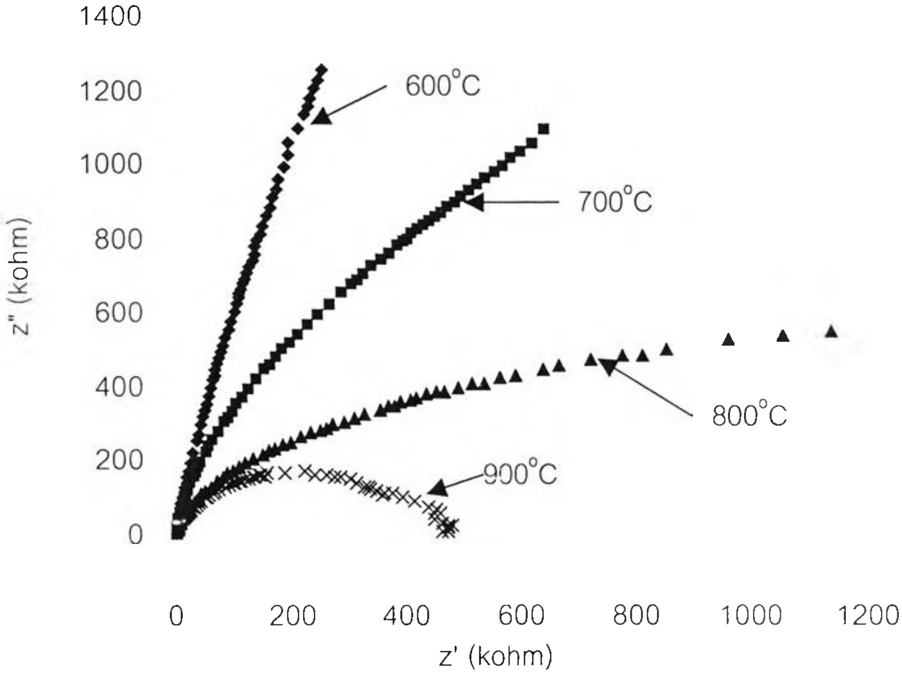

Fig.4.14(b) Impedance plots of std at 600-900°C

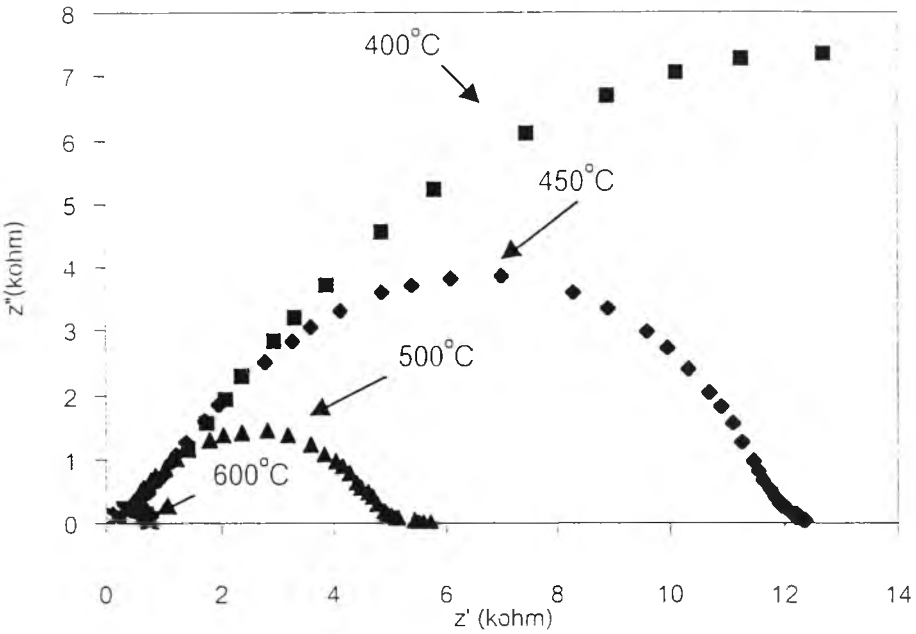

Fig 4.15 Impedance plots of S10 at 400-600°C

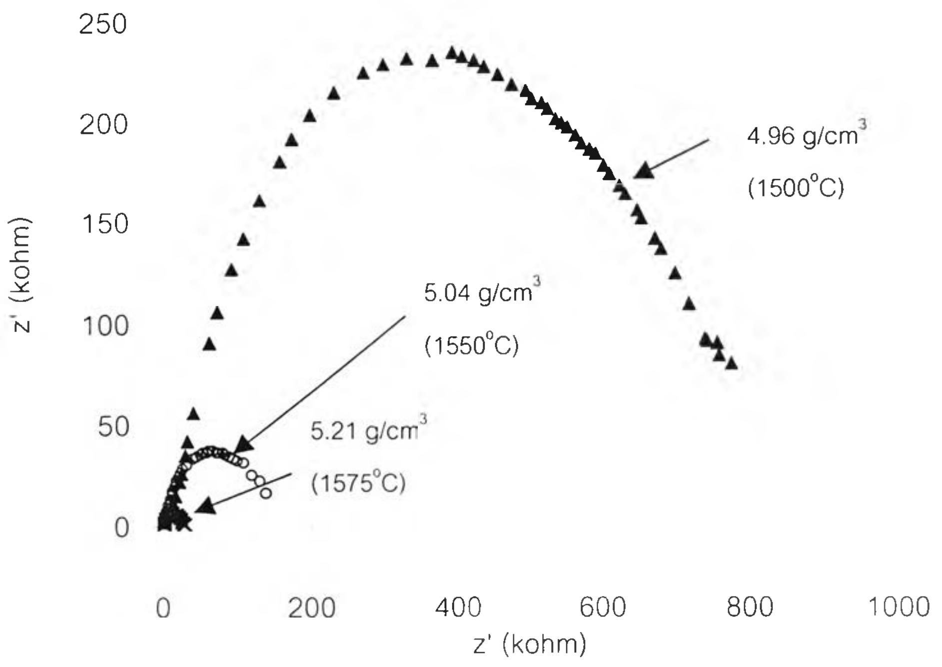

Fig 4.16 Impedance plots of S10 sintered at 1500, 1550 and 1575°C and the bulk density at each sintering temperature.

The conductivity was obtained from equation 4.4

$$\sigma = \frac{l}{RA} \qquad (4.4)$$

when l is the distance between two electrodes, A is the electrode area and R is obtained from interception of the z' axis. The Arrhenius plots of S5 sintered at 1500°C, S10 and S15 sintered at 1575°C were shown in Fig 4.17. Also, the plots of M5, M10 and M15 sintered at 1575°C were shown in Fig 4.18. Similar to results of DC measurement, the activation energy decreased with increasing temperature. The two straight lines of each composition were determined by fitting to a regression coefficient greater than 0.997 and illustrated in Fig 4.19 and 4.20. The activation energy and the conductivity of all compositions calculated from the plots in Fig. 4.19 and 4.20 were summarized in Table 4.7 and 4.8.

Table 4.7 Calculated activation energy of S5, S10 and S15 by AC impedance as a function of composition.

Composition	Temperature range (°C)	E_a (kJ/mol)
S5	350-550	131
	550-800	112
S10	350-450	124
	450-800	104
S15	350-600	200
	600-800	135
M5	350-550	132
	550-800	105
M10	350-450	136
	450-800	104
M15	350-520	128
	520-800	97

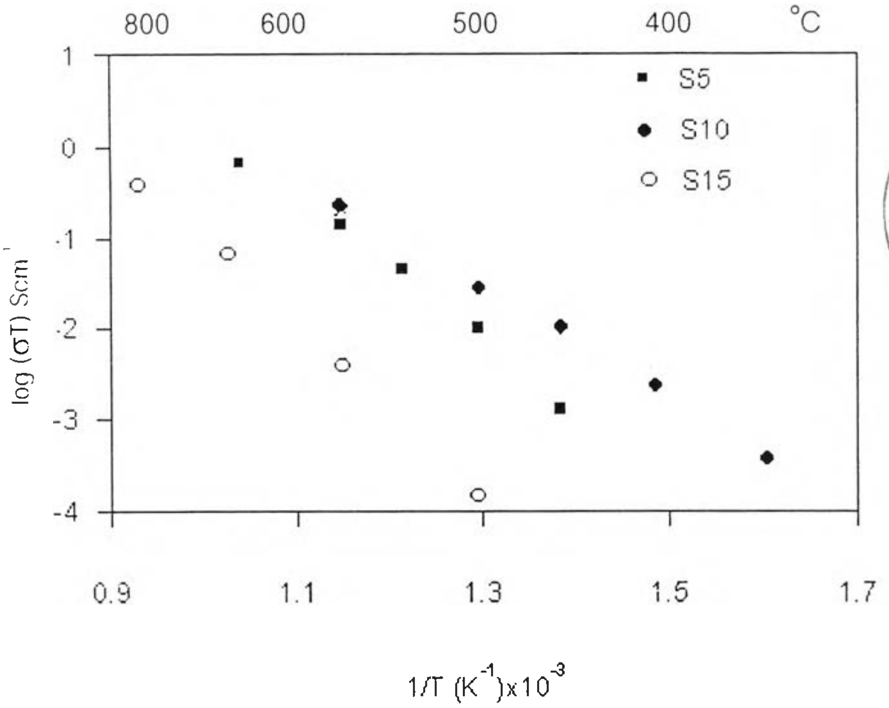

Fig 4.17 AC conductivity vs reciprocal temperature of S5 sintered at 1500°C, S10 and S15 sintered at 1575°C

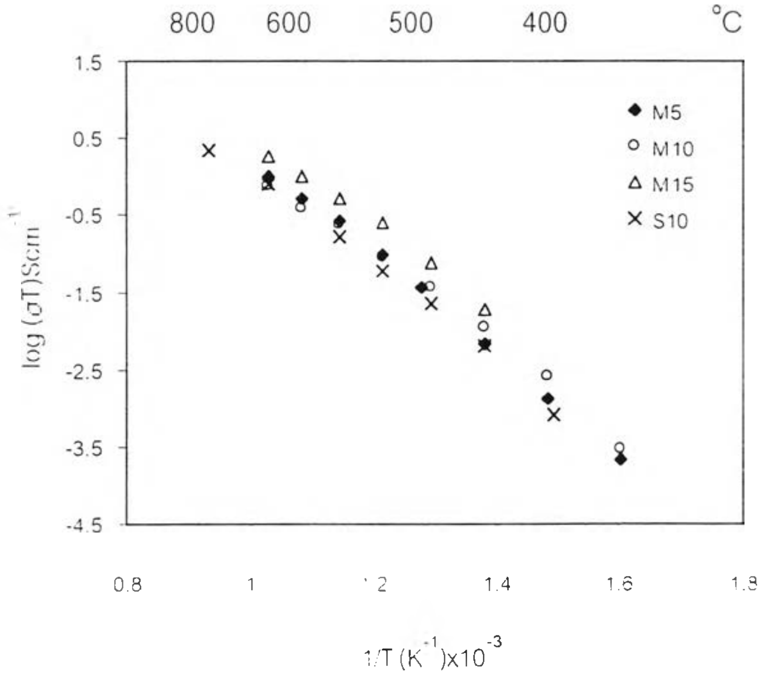

Fig 4.18 AC conductivity vs reciprocal temperature of S10, M5, M10 and M15 sintered at 1575°C

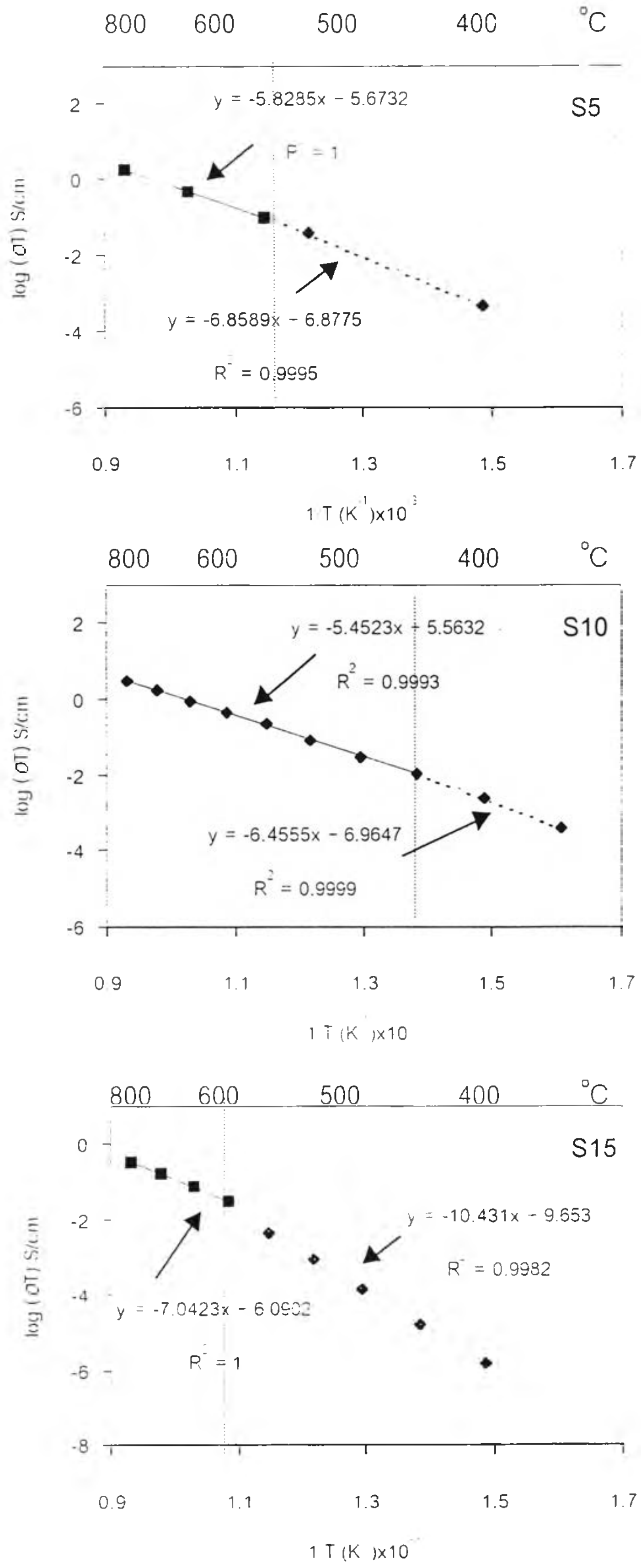

Fig 4.19 AC conductivity vs reciprocal temperature of S5, S10 and S15 illustrated the two straight lines with the equation and the regression coefficient

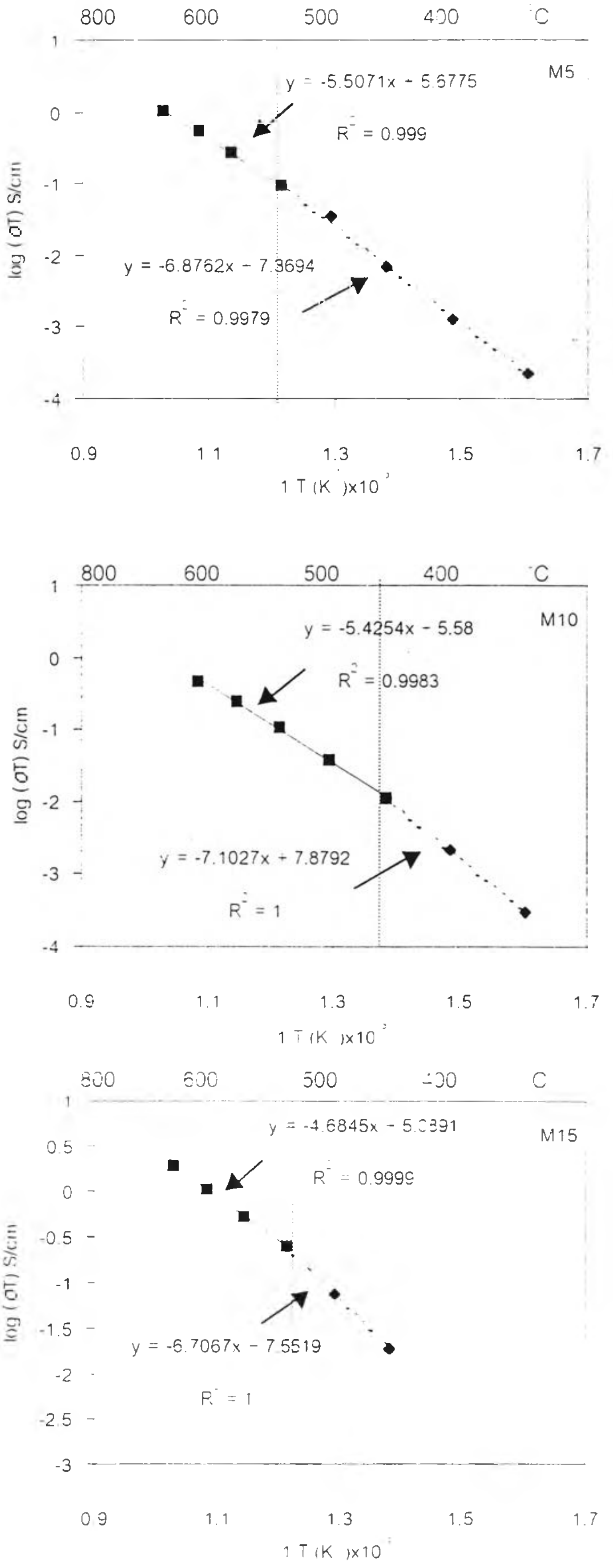

Fig 4.20 AC conductivity vs. reciprocal temperature of M5, M10 and M15 illustrated the two straight lines with the equation and the regression coefficient.

Table 4.8 Calculated σ_{1000} and σ_{800} of S5, S10 and S15 by AC impedance as a function of composition.

Composition	σ_{1000} (S/cm)	σ_{800} (S/cm)
S5	9.77×10^{-3}	1.62×10^{-3}
S10	14.97×10^{-3}	2.83×10^{-3}
S15	2.84×10^{-3}	0.31×10^{-3}
M5	15.57×10^{-3}	2.96×10^{-3}
M10	16.34×10^{-3}	3.11×10^{-3}
M15	301.06×10^{-3}	37.23×10^{-3}

Similar to the result of dc measurement, the activation energy decreased as the temperature increased. This type of phenomenon had been observed in other ionic conductors.

i) Effect of the Sr content

It was evident that the electrical conductivity tended to increase as the amount of Sr increased. However, when the Sr content was up to 15mol%, the conductivity decreased. S10 had the highest electrical conductivity of 14.93×10^{-3}S/cm at 1000°C and 2.83×10^{-3} S/cm at 800°C, corresponding to the result of dc measurement. σ_{1000} and σ_{800} of S15 were the lowest value of electrical conductivity, 2.84×10^{-3} S/cm and 0.31×10^{-3} S/cm, respectively. The low conductivity of S15 possibly resulted from its high activation energy due to the presence of second phase.

ii) Effect of Mg content

The results of the activation energy and the temperature dependence on the conductivity of pellet sintered at 1575°C 4 h of M5, M10 and M15 were summarized in Table 4.7 and 4.8, respectively. The electrical conductivity of M5, M10 and M15 was higher than that of S10, although their activation energy at the high temperature was slightly different. The conductivity increased with the amount of Mg, especially 15mol% of Mg. The σ_{1000} and σ_{800} of M15 approached 301.06×10^{-3} S/cm and 37.23×10^{-3} S/cm, respectively. The reason for this was possibly due to the large amount of dopants creating the higher oxygen vacancies concentration resulting in the higher conductivity. The conductivity of M15 was higher than that of YSZ (0.1 S/cm at 1000°C).

The conductivity of dc and ac measurements were compared in Table 4.9. Since Sr substituted in $LaAlO_3$ were measured by both dc and ac; therefore only S5, S10 and S15 were shown.

Table 4.9 The σ_{1000} and σ_{800} of S5, S10 and S15 from dc and ac methods.

Composition	σ_{1000} (S/cm)		σ_{800} (S/cm)	
	dc	ac	dc	Ac
S5	9.42×10^{-3}	9.77×10^{-3}	1.64×10^{-3}	1.62×10^{-3}
S10	10.35×10^{-3}	14.97×10^{-3}	1.85×10^{-3}	2.83×10^{-3}
S15	8.90×10^{-3}	2.84×10^{-3}	1.47×10^{-3}	0.31×10^{-3}

It could be concluded from Table 4.9 that the σ_{1000} and σ_{800} which were measured by dc method were not different. While the result from ac method had a significant difference. In addition, the σ_{1000} of S10 measured by ac impedance was in good agreement with that reported by Nomura K. (8) (15.8 $Sx10^{-3}cm$).

4.5.4 Microstructure

The microstructures of the specimens were examined by the scanning microscope (SEM). Fig 4.21-4.25 showed the SEM micrographs of all polished and thermal etched samples. Fig 4.21 showed that the sintered $LaAlO_3$ composition had the average grain size larger than 1 micron. With 5mol% of Sr (S5), the grain growth was inhibited the average grain size was much smaller than that of undoped composition as in Fig 4.22. In addition, pores could be observed through the polished sample, resulting low density as compared to that of std. That was also in good agreement with the result of bulk density from Archimedes method in Table 4.4. Similar to S5, intergranular pores were observed in S10 and the average grain size was larger at the sintering temperature of 1575°C. The SEM analysis of S15 (Fig 4.23) revealed a dense sample composed of two phases. The inhomogeneous of the substitution of Sr has been published by Anderson P.S. (9). The dark grains reported were rich in Al and Sr with low La content. The amount of the second phase increased with the amount of Sr-dopant.

4.5.5 Thermal expansion coefficient

A dilatometer was used to determine the thermal expansion coefficient of sintered specimens. All compositions exhibited linear thermal expansion coefficient from room temperature to 900°C. The results were calculated and listed in Table 4.10

Table 4.10 Thermal expansion coefficient (TEC) of std, S5 sintered at 1500°C and S10, S15, M5, M10 and M15 sintered at 1575°C

Composition	TEC(100-900°C) x 10^{-6}(K^{-1})
Std	10.52
S5	11.37
S10	11.57
S15	11.92
M5	11.58
M10	11.67
M15	11.93

The measured TEC of std in this experiment was slightly different from the study of Vanderah (1) (11-12 x10^{-6}K^{-1}). The TEC increased as Sr content increased. Also, the substitution with Mg caused higher thermal expansion and the TEC increased with the amount of Mg. The TEC of all compositions except std was higher than that of YSZ (10.5x10^{-6} K^{-1}). The TEC of M15 which provided the maximum electrical conductivity was closed to the TEC of the most common cathode (1) ($La_{0.9}Sr_{0.1}MnO_3$ 12x10^{-6} K^{-1}). Thus this composition was acceptable for using with LSM cathode.

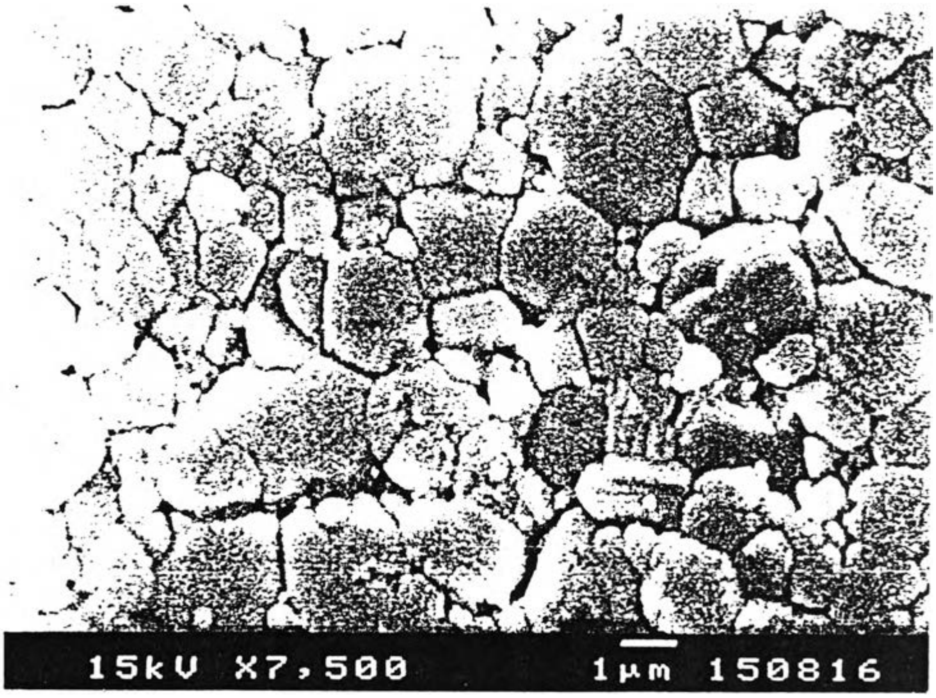

Fig 4.21 SEM micrograph of std sintered at 1500°C

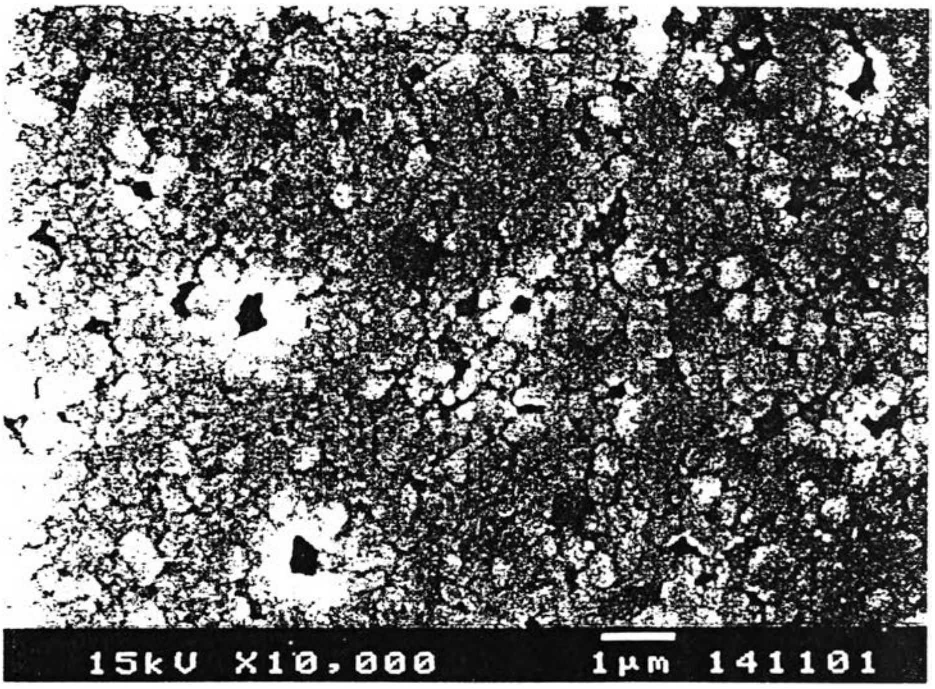

Fig 4.22 SEM micrograph of S5 sintered at 1500°C

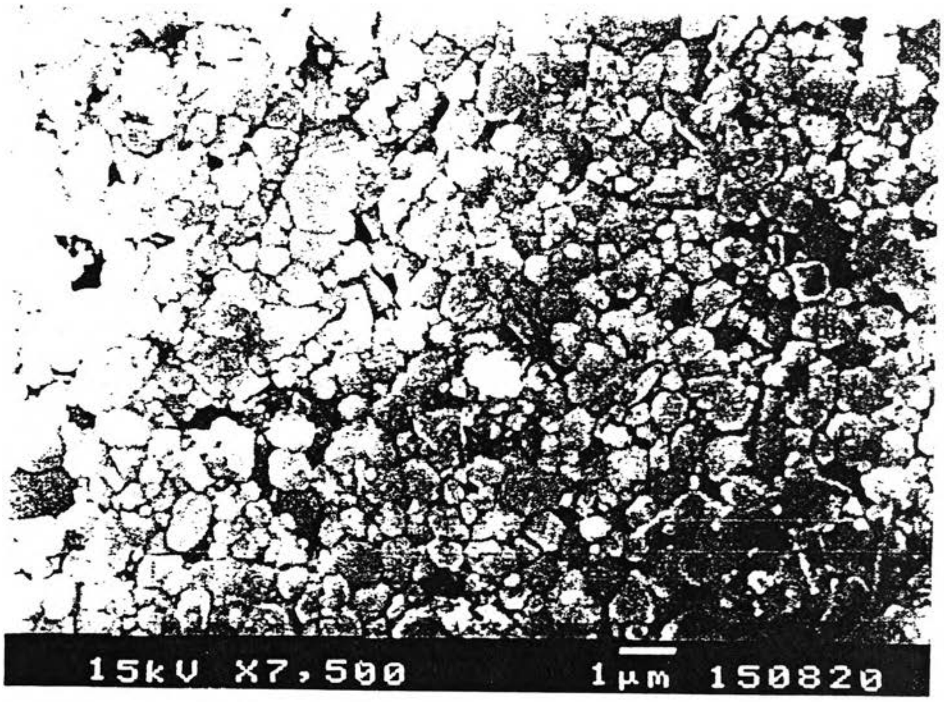

Fig 4.23 SEM micrograph of S10 sintered at 1575°C

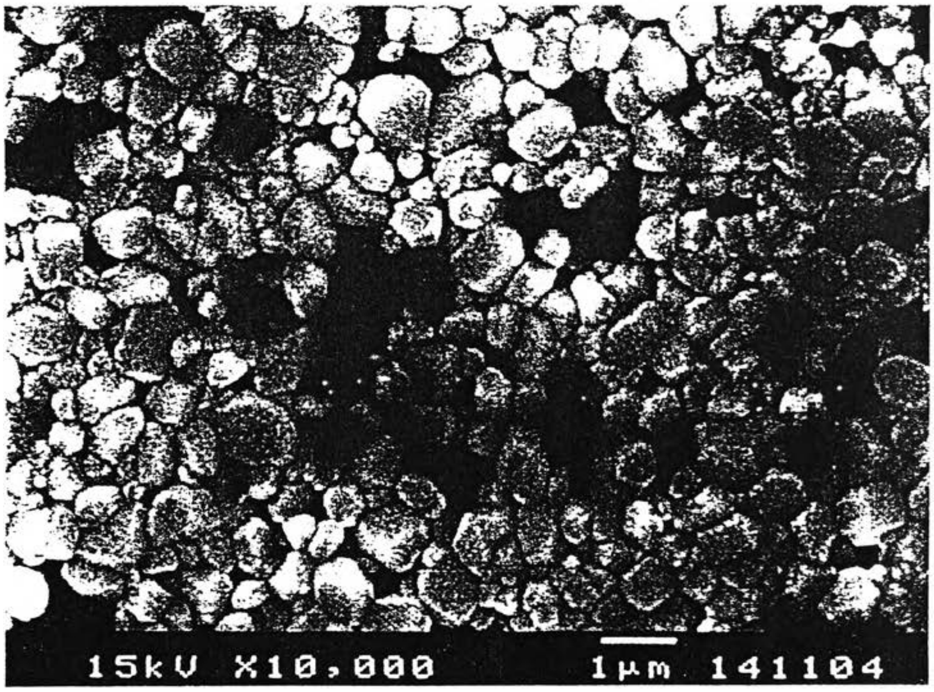

Fig 4.24 SEM micrograph of S15 sintered at 1575°C

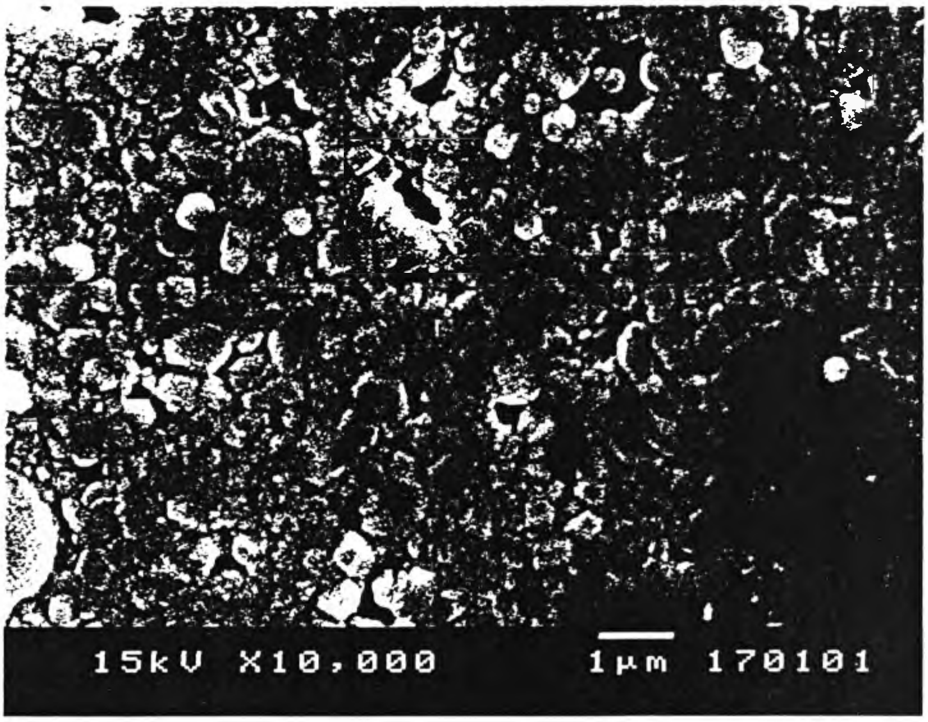

Fig 4.25 SEM micrograph of M15 sintered at 1575°C